

RESEARCH ARTICLE

10.1002/2013JA019583

Key Points:

- F region density cavities result from strong electric fields
- Cavities are largely due to recombination
- Model results and ISR data are consistent

Correspondence to:

M. Zettergren,
zettergm@erau.edu

Citation:

Zettergren, M., K. Lynch, D. Hampton, M. Nicolls, B. Wright, M. Conde, J. Moen, M. Lessard, R. Miceli, and S. Powell (2014), Auroral ionospheric F region density cavity formation and evolution: MICA campaign results, *J. Geophys. Res. Space Physics*, 119, 3162–3178, doi:10.1002/2013JA019583.

Received 30 OCT 2013

Accepted 7 MAR 2014

Accepted article online 12 MAR 2014

Published online 17 APR 2014

Auroral ionospheric F region density cavity formation and evolution: MICA campaign results

M. Zettergren¹, K. Lynch², D. Hampton³, M. Nicolls⁴, B. Wright¹, M. Conde³, J. Moen⁵, M. Lessard⁶, R. Miceli⁷, and S. Powell⁷

¹Physical Sciences Department, Embry-Riddle Aeronautical University, Daytona Beach, Florida, USA, ²Physics Department, Dartmouth College, Hanover, New Hampshire, USA, ³Geophysical Institute, University of Alaska Fairbanks, Fairbanks, Alaska, USA, ⁴SRI International, Menlo Park, California, USA, ⁵Department of Physics, University of Oslo, Oslo, Norway, ⁶Department of Physics, University of New Hampshire, Durham, New Hampshire, USA, ⁷Electrical and Computer Engineering Department, Cornell University, Ithaca, New York, USA

Abstract Auroral ionospheric F region density depletions observed by PFISR (Poker Flat Incoherent Scatter Radar) during the MICA (Magnetosphere-Ionosphere Coupling in the Alfvén Resonator) sounding rocket campaign are critically examined alongside complementary numerical simulations. Particular processes of interest include cavity formation due to intense frictional heating and Pedersen drifts, evolution in the presence of structured precipitation, and refilling due to impact ionization and downflows. Our analysis uses an ionospheric fluid model which solves conservation of mass, momentum, and energy equations for all major ionospheric species. These fluid equations are coupled to an electrostatic current continuity equation to self-consistently describe auroral electric fields. Energetic electron precipitation inputs for the model are specified by inverting optical data, and electric field boundary conditions are obtained from direct PFISR measurements. Thus, the model is driven in as realistic a manner as possible. Both incoherent scatter radar (ISR) data and simulations indicate that the conversion of the F region plasma to molecular ions and subsequent recombination is the dominant process contributing to the formation of the observed cavities, all of which occur in conjunction with electric fields exceeding ~ 90 mV/m. Furthermore, the cavities often persist several minutes past the point when the frictional heating stops. Impact ionization and field-aligned plasma flows modulate the cavity depth in a significant way but are of secondary importance to the molecular generation process. Informal comparisons of the ISR density and temperature fits to the model verify that the simulations reproduce most of the observed cavity features to a reasonable level of detail.

1. Introduction

Depletions in F region plasma density in the mid-latitude and high-latitude regions are commonplace, particularly at night. The mid-latitude trough occurs equatorward of the main auroral zone, typically on the nightside during winter or equinox conditions (see reviews by Moffett and Quegan [1983] and Rodger *et al.* [1992, and references therein]). Mid-latitude troughs also commonly form in disturbed regions of subauroral ion drifts, large nightside, westward plasma flows which last for several hours and have speeds of 0.5–4 km/s [e.g., Anderson *et al.*, 1991; Karlsson *et al.*, 1998]. Troughs in the auroral zone are also often observed and are typically several degrees wide in latitude. These troughs usually have elevated ion temperatures [Winser *et al.*, 1986] and unusually large relative concentrations of molecular ions [Grebowsky *et al.*, 1983]. Observations have shown that the high-latitude trough often occurs eastward of the Harang reversal region [Zou *et al.*, 2013, and references therein]. Both mid-latitude and high-latitude troughs typically move equatorward during enhanced geomagnetic activity [e.g., Collis and Haggstrom, 1988], and their formation and dynamics are sometimes associated with substorms [Evans *et al.*, 1983; Zou *et al.*, 2013]. At high latitudes, transient auroral density cavities sometimes form in regions adjacent to nightside auroral arcs [Doe *et al.*, 1993]. These density cavities typically involve intense ion heating and are thought to be coincident with the return current channel of the auroral arc [Doe *et al.*, 1993; Aikio *et al.*, 2004; Nilsson *et al.*, 2005; Zettergren *et al.*, 2010]. Finally, in the polar cap during wintertime, a polar “density hole” may form due to long residency time of plasma in regions with weak or no photoionization [e.g., Brinton *et al.*, 1978; Sojka *et al.*, 1981a].

It has long been recognized that high-latitude $\mathbf{E} \times \mathbf{B}$ convection plays a critical role in creating and regulating plasma density structures [cf. Rodger *et al.*, 1992, and references therein]. Competition between plasma

corotation and convection in subauroral regions can lead to extended nighttime residency of plasma in the dusk sector and low plasma densities [Knudsen, 1974]. Modeling results have confirmed that this mechanism contributes substantially to the formation of the mid-latitude trough [Sojka *et al.*, 1981a, 1981b]. Lifetime of density enhancements and depletions can be altered by convection through regions that are sunlit or subjected to energetic particle fluxes. Variable convection can also distort existing features or fracture them into smaller structures [e.g., Schunk and Sojka, 1987]. Some studies have suggested that, despite the obvious role that structured convection plays in large-scale density depletions, it is not sufficient to explain the formation of many arc-related density cavities [Doe *et al.*, 1994].

Aside from slow convection of plasma through regions not illuminated by solar flux, a variety of mechanisms can actively deplete the ionospheric plasma at high latitudes [cf. Zettergren and Semeter, 2012, section 1 for a detailed account]. Enhanced charge exchange due to frictional heating from strong $\mathbf{E} \times \mathbf{B}$ drift is capable of partially converting *F* region ions into molecular ions which quickly recombine [Schunk *et al.*, 1975; Diloy *et al.*, 1996]. Indirect incoherent scatter radar (ISR) observations have suggested that this mechanism can be efficient for auroral arc electric fields ≥ 75 –100 mV/m [Kelly and Wickwar, 1981; Haggstrom and Collis, 1990; Zettergren *et al.*, 2011]. Moreover, many satellite observations of troughs and depletions have suggested the presence of molecular ions in ionospheric density cavities [Grebowsky *et al.*, 1983; Wilson and Craven, 1999].

E region plasma depletions in auroral downward current regions (DCRs) can result from divergent ion Pedersen drifts. Both electrostatic [Doe *et al.*, 1995; Karlsson *et al.*, 2005; Marklund, 2009; de Boer *et al.*, 2010] and electrodynamic [Cran-McGreehin *et al.*, 2007] modeling have confirmed the efficiency of this process, which has also been linked to ionospheric feedback [Russell *et al.*, 2013] and feedback instability [Lysak and Song, 2002; Streltsov and Lotko, 2004]. These feedback effects may be capable of explaining intense small-scale Alfvénic current structures often observed in auroral current systems [Streltsov and Karlsson, 2008]. In general, this evacuation process is thought to be most efficient for small-scale current systems or those that transition sharply from upward to downward current [Zettergren and Semeter, 2012].

Phenomena associated with auroral arc-related density depletions are likely to interact in significant ways. Zettergren and Semeter [2012] have presented a study of the combined effects of current closure, enhanced recombination, and strong ion upflows in auroral DCRs subjected to intense frictional heating. Their results show that, in current systems of ≥ 20 km scale size, enhanced recombination is likely to play the dominant role of depleting the DCR *F* region. Moreover, they have demonstrated that the simultaneous action of all of these depletive processes produces effects consistent with those observed in connection with *F* region density cavities (DCR broadening, plasma depletions extending from 120 to 600 km). As another example of coupling of depletion processes, DCR depletion and ionospheric feedback instability may lead to intense electromagnetic fluctuations which ponderomotively lift and evacuate the lower *F* region [Streltsov and Lotko, 2008].

Zettergren and Semeter [2012] have made several simplifying assumptions in their modeling; hence, their conclusions are necessarily of limited scope. First, they have largely neglected the effects of precipitating electrons in the upward current regions (UCRs). UCR precipitation will be of consequence to ionospheric densities in the *F* region (see also work by de Boer *et al.* [2010]) but is difficult to study owing to the *ad hoc* nature in which the field-aligned currents and precipitating particles are specified as boundary conditions to the models. The second issue is that Zettergren and Semeter [2012] predominantly used a simple up-down current system where applied electric fields varied smoothly from one current region to another. In reality, conductivities, fields, and heating are likely to vary sharply at the UCR/DCR boundary [e.g., Noël *et al.*, 2000]. Furthermore, the current system itself may be more complicated in many situations, perhaps containing several up-down current pairs, and is most likely also in motion.

This paper presents new observations of plasma depletions during the MICA (Magnetosphere-Ionosphere Coupling in the Alfvén Resonator) sounding rocket campaign, including details of their formation, evolution, and decay. We aim to use data recorded during the MICA experiment to improve the studies of Zettergren and Semeter [2012] by examining the effects of variable auroral drivers (fields and particles) on ionospheric depletions. The focus for this paper is on the large-scale ionospheric features before, during, and after the MICA flight, while other related articles will explore the fine-scale features observed in situ (K. A. Lynch *et al.*, Observations of gradient-generated auroral ionospheric response effects as seen by the MICA sounding rocket, *Journal of Geophysical Research*, In preparation, 2014) and new auroral particle estimation techniques (D. L. Hampton, *et al.*, Detailed regional auroral electron energy deposition estimations using measurements

of E-region temperature and N_2^+ first-negative emissions: A MICA case study, *Journal of Geophysical Research*, In preparation, 2014). For our large-scale study, the approach is to *completely* rely on data from optical and ISR systems to constrain particle precipitation and electric field boundary conditions for the model. This guiding principle leads to the development of a model/data analysis framework which may also be useful for other experiments with combined ISR and optical data. Furthermore, it allows verification of the model since the simulated ionospheric state may be compared against the PFISR observations of density and temperature (which are not used to drive the model). Aside from details of formation due to frictional heating and current closure loss, considerable attention is paid to possible effects of transient ion upflows and neutral winds on density cavity formation.

2. PFISR Observations

The MICA sounding rocket was launched from Poker Flat, AK, on 19 February 2012 at 5:41:06.745 UT, into a substorm expansion aurora. The flight lasted for 552 s and had an apogee of ~ 325.4 km. Among other parameters, MICA made detailed observations of thermal plasma density and electron temperature. Complementary ISR, Fabry-Perot, and all-sky camera measurements were made from ~ 2 to 8 UT. The MICA PFISR experiment consisted of a set of 15 beams arranged in a manner somewhat similar to the experiment of Zou *et al.* [2013] (see also Figure 5). Both long pulse (processed at 1 min and 3 min integration) and alternating code (3 min integration) were used, though we focus primarily on the long pulse data. The substorm breakup which prompted the call to launch occurred at $\sim 5:40$ UT.

Before presentation and discussion of the ISR results, it is worthwhile to review a few details concerning the processing of incoherent scatter (IS) spectra into the plasma parameters n_e , T_i , T_e , and v_i . The fundamental ISR measurements are spectra of plasma density fluctuations associated with ion-acoustic waves [e.g., Evans, 1969]. To produce the plasma parameter estimates, a model containing these parameters is fitted to the observed autocorrelation function. The chief assumptions behind the IS spectral model are that (1) the ion distribution function is suitably described by a drifting Maxwellian and (2) the ion mass can be specified in a reasonably accurate way. Deviations from the Maxwellian model are numerous and well-known [cf. Zettergren *et al.*, 2011, sections 1 and 2 and references therein]. In particular, the interpretation of spectra during strong frictional heating for aspect angles (the angle between the ISR beam and local geomagnetic field) $> 30^\circ$ is fraught with complications [Raman *et al.*, 1981; Hubert and Lathuillere, 1989]. Moreover, various plasma instabilities at high latitudes also distort IS spectra [e.g., Akbari *et al.*, 2012]. Finally, ion mass/composition at high latitudes is known to be highly variable which may result in errors in derived temperatures [e.g., Zettergren *et al.*, 2010, and references therein].

For the present study, one of the main concerns is the effects of molecular ions on temperature fits. Molecular ions are readily generated in the *F* region when it is subjected to intense frictional heating [Schunk, 1977; St.-Maurice and Laneville, 1998; Diloy *et al.*, 1996; Zettergren and Semeter, 2012]. If not properly accounted for in the fitting procedure, these molecular ions can result in erroneously low-temperature estimates [Zettergren *et al.*, 2010]. The data shown in this section are processed using a method based on the Ion Density Calculator (IDC) of Richards *et al.* [2010], which is able to specify ion composition under certain assumptions. Though it is not clear a priori that this technique will be accurate in regions of intense heating, we demonstrate that the results are roughly consistent with theoretical expectations.

The ISR beam pattern used for the MICA experiment is such that 10 of the 15 beam positions have aspect angles of greater than 30° . During times of intense frictional heating, spectra observed from these positions *will* have a non-Maxwellian character. Thus, we expect the fitted parameters, composition issues notwithstanding, to deviate from their true values when the electric fields are large (greater than ~ 75 mV/m) [Raman *et al.*, 1981]. Following the calculations of Raman *et al.* [1981], it is noted that the density may be overestimated by as much as 15%, the ion temperatures may be overestimated by as much as $\sim 50\%$, and the electron temperatures may be underestimated by up to $\sim 50\%$ (these ranges are only approximate).

2.1. Density Cavities During MICA Experiment

Perhaps the most remarkable feature of the ISR data is the intermittent appearance of density cavities extending through the *E* and *F* regions to the north of the radar. Cavity events were extracted from the ISR data by visually identifying structures that (1) are extended in longitude (greater than ~ 100 km) and altitude ($> \sim 50$ km), (2) have at least one well-defined edge with a sharp density gradient, (3) are temporally coherent (present in at least two consecutive integration periods), and (4) have depletions of $\sim 20\%$ or more

Table 1. Cavity Events Identified From the MICA ISR Experiment^a

Event	Cavity Visibility	Heating Duration	Comments
1	2:48–3:10 UT	2:20–3:10 UT	arc in field of view after 3:10
2	3:56–4:21 UT	3:50–4:10 UT	two separate cavities appearing consecutively
3	4:59–5:33 UT	4:50–5:10 UT	not clearly visible after 5:33 UT
4	6:26–6:32 UT	6:15–6:30 UT	possibly obscured by arc after 6:32
5	7:38–7:50 UT	7:35–7:45 UT	exists until end of ISR experiment

^aFor reference, the MICA time of flight is ~5:41:07 to 5:50:18 UT. Note that none of these events encompass the MICA flight times, though event 3 may have had some remnant present during the flight (cf. Figure 11).

relative to the maximum density adjacent to the cavity. As discussed below each event was accompanied by frictional heating. The duration of this heating (again, assigned visually) is taken to be the times when the fitted ion temperature (1) exceeds ~3000 K, (2) is coherent spatially (roughly extending from 200 to 300 km in altitude), and (3) exists in at least two consecutive integrations. A listing of event times and accompanying frictional heating duration is shown in Table 1.

Figure 1 shows a collection of electron density estimates from events 1–2 and 4–5 (event 3 is examined in more detail below). Note the presence of depleted density regions (~35–75% less than surrounding regions) extending from the 150 to 300 km planes, morphologically similar to observations by *Doe et al.* [1993]. In each of the cases shown the density depletions are collocated with regions of ion temperature (not shown) with fitted values of >3000–5000 K in the 300 km altitude plane, while the temperatures outside the cavities

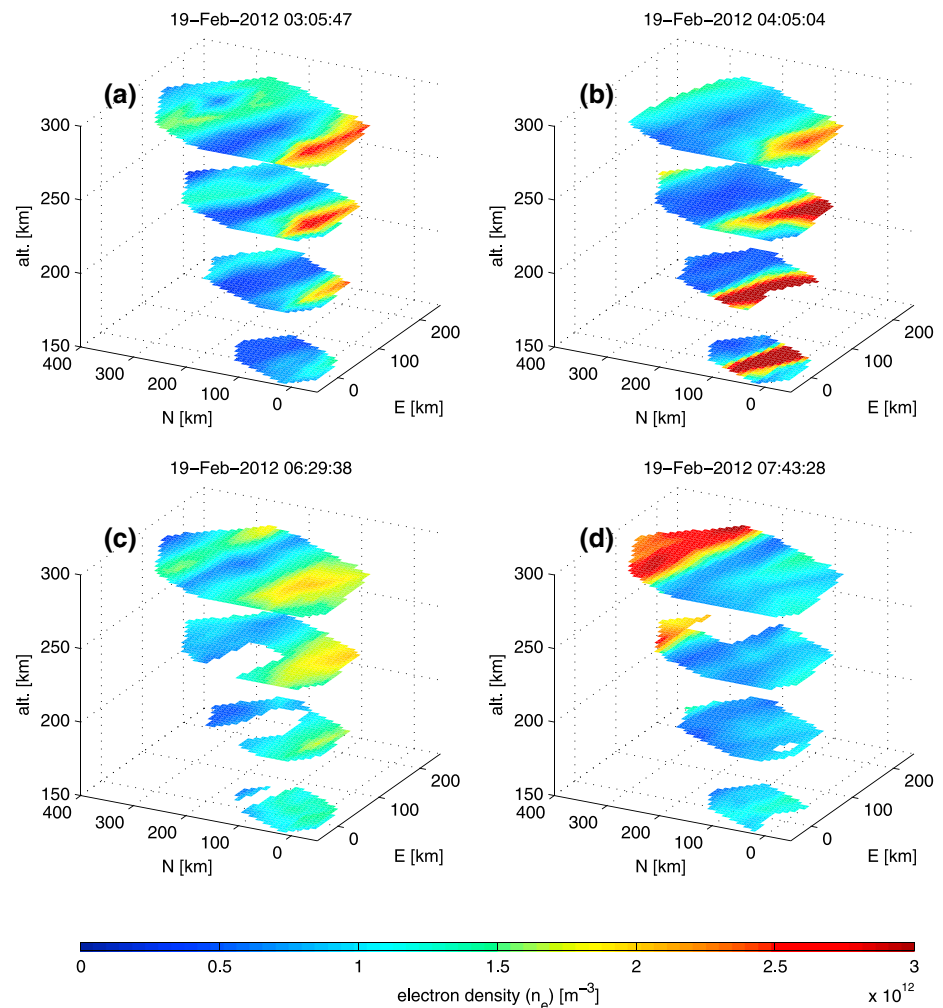


Figure 1. Electron density measurements showing cavities intermittently observed during the 19 February 2012, 2–8 UT ISR experiment. (a) Event 1 (3:05 UT), (b) event 2 (4:05 UT), (c) event 4 (6:30 UT), and (d) event 5 (7:45 UT).

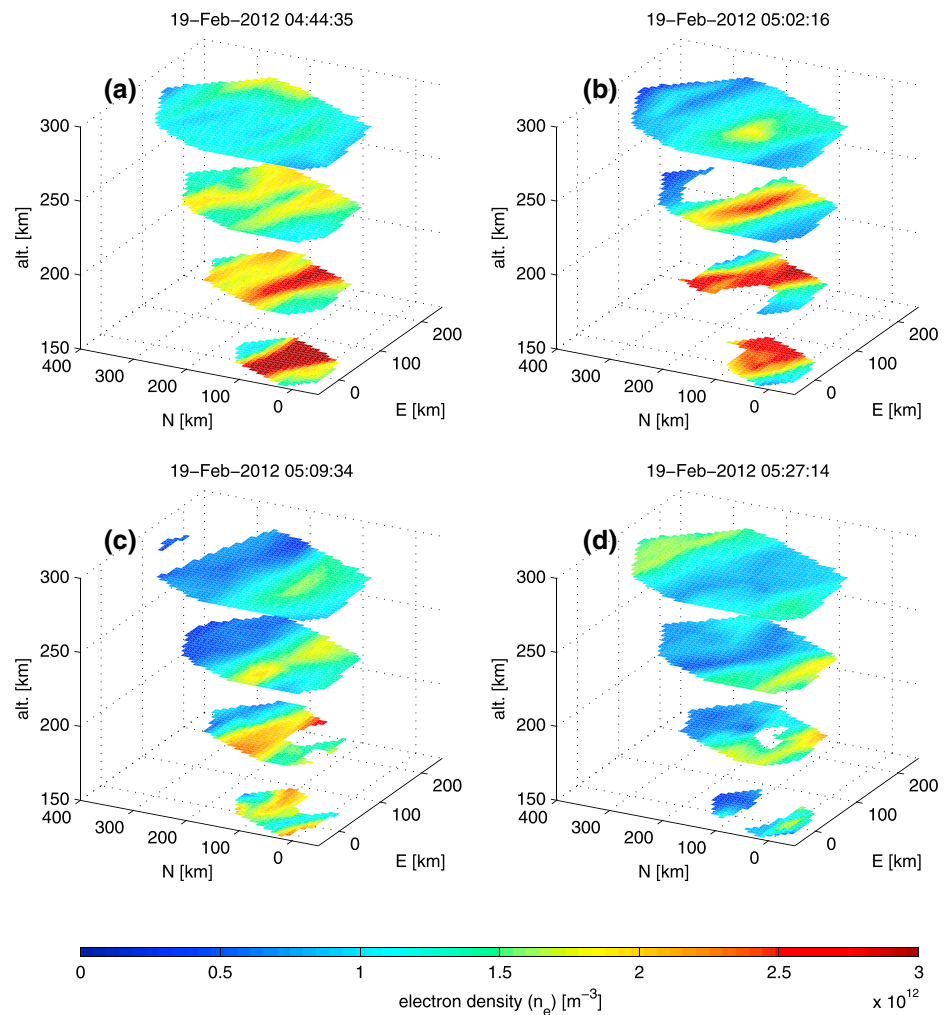


Figure 2. Electron density depletion evolution around the times of event 3 (~4:59–5:33 UT). (a) Density before frictional heating and cavity appearance (4:44:35 UT). (b) Cavity during the time corresponding to peak frictional heating (5:02:16 UT). (c) Cavity right before the heating ends (5:09:34 UT). (d) Cavity ~10 min before the substorm surge (5:27:14 UT).

are ~1250 K. Fitted electron temperatures in the depleted regions (not shown) are somewhat low, ~800 K, compared to ~2250 K outside the cavities. PFISR electric field estimates for all cases are in excess of 90 mV/m, either during the cavity observation or immediately preceding it. Examination of the 150 km plane cut in each panel shows that the depletions occur just outside a region of substantial impact ionization.

Another ionospheric density cavity appeared in the radar scans around ~4:59 UT and was visible until ~5:33 UT (event 3). Figures 2 and 3 show the temporal evolution of this cavity in terms of fitted density and ion temperature from the time before the heating began (Figures 2a and 3a) until ~10 min before the substorm surge (Figures 2d and 3d). It can be seen from Figure 2 that the cavity here has the same character as those presented in the previous figure, namely, it appears as an extended structure spanning both *E* and *F* regions. A glance at Figures 2d and 3d reveals that the density depletion outlasts the ion frictional heating. Enhanced ion temperatures associated with this cavity last from about 4:50 to 5:10 UT, whereas the cavity clearly persists up until at least ~5:33 UT. This behavior is to be expected when there is not a significant ionization source in the cavity. The depleted region has a slight equatorward apparent motion following the intense ion heating (compare Figures 2c and 2d). A modest westward electric field of ~10 mV/m, which appeared near the northern edge of the ISR field of view around ~5:20 UT and moved southward may be responsible for this motion (see Figure 6b). As a rough estimate, the $\mathbf{E} \times \mathbf{B}$ drift speed for this observed field would be about 208 m/s, while the cavity is observed to move ~200 km in about 10 min, an apparent drift speed of ~333 m/s. Another process possibly contributing to this apparent motion is that the region of strong (~75 mV/m) northward electric field moved southward from 5:05 to 15 UT before disappearing

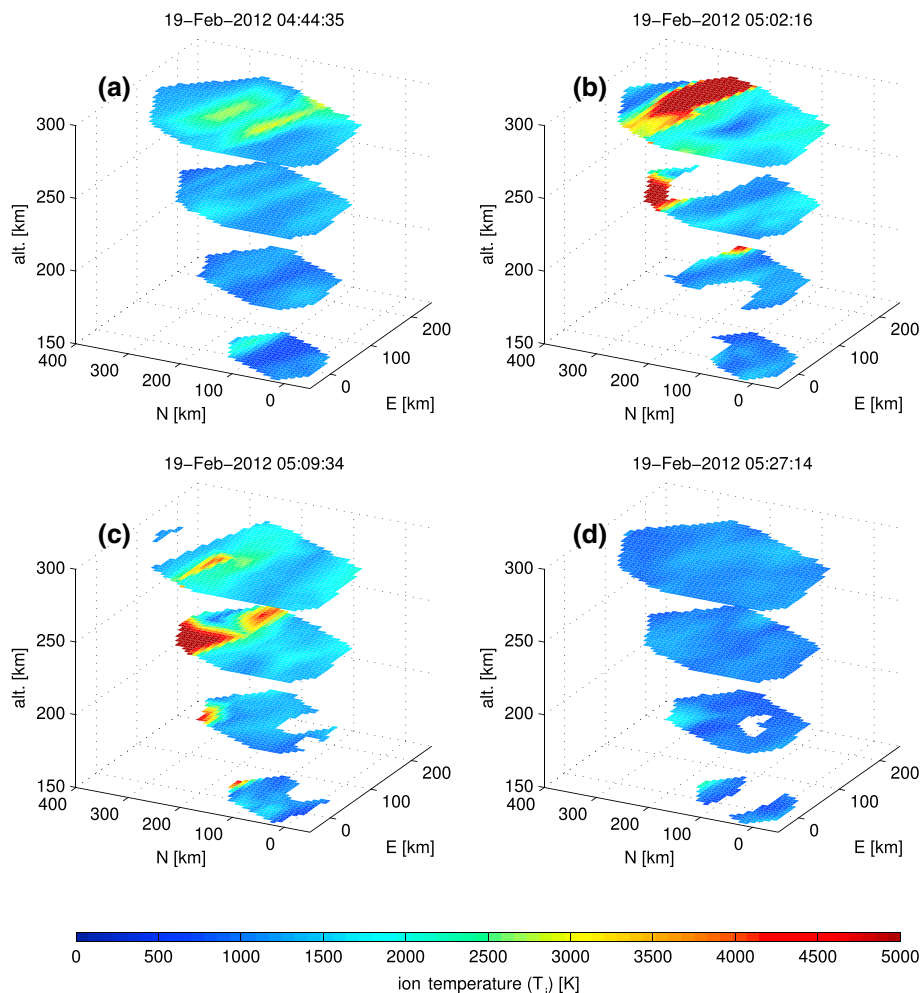


Figure 3. Ion temperature evolution for event 3. Same panel times as in Figure 2.

(Figure 6a), which may have produced molecular ions in the region south of the existing cavity. These molecules would later recombine to yield some apparent southward motion. Finally, it is noted that this is not the strongest event in the data set; however, it is examined here due to its temporal proximity to the MICA launch.

2.2. Molecular Ion Estimates

Molecular ion generation during the heating from 4:56 to 5:09 UT (event 3) is examined now using PFISR data processed through a technique based on the IDC (ion density calculator) method described in *Richards et al.* [2010]. This method uses measured electron density profiles (not subject to composition errors) to find a consistent chemical equilibrium solution for ion densities. These fits proceed iteratively for each set of spectra while adjusting the ISR parameters (n_e , T_e , T_i , and v_i) for the newly inferred ion composition (assuming chemical equilibrium for molecular species), until convergence is achieved. Hence, IDC does take into account highly temperature sensitive charge-exchange reaction rates [*McFarland et al.*, 1973; *Torr et al.*, 1977; *St.-Maurice and Torr*, 1978; *St.-Maurice and Laneville*, 1998]. The validity of this approach is difficult to evaluate in the context of evolving auroral flow conditions. However, observed heating events lasted at least 10 min (Table 1) so the chemical equilibrium may be expected to produce reasonable results. In any case, our purpose here is merely to present these estimates and to evaluate their consistency with the model results in later sections.

Figure 4 shows ion composition during the 5:09:34 and 5:27:14 UT PFISR scans (around the time of event 3). At 5:09:34 UT the ionosphere was being actively heated due to the strong $\mathbf{E} \times \mathbf{B}$ drifts. Molecular ion enhancements near the northern edge of the field of view are clearly visible in the 200–250 km regions.

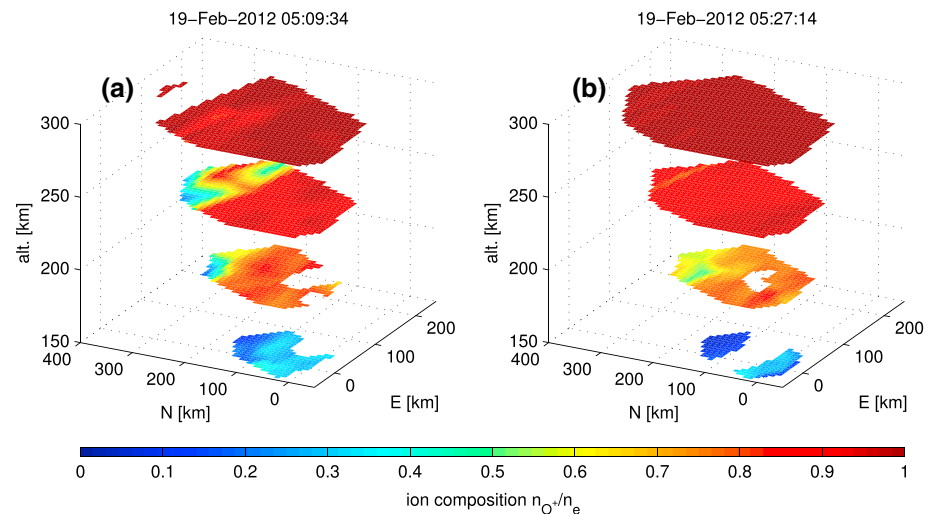


Figure 4. Ion composition during event 3 estimated from IDC procedure. (a) Composition shows significant concentrations of molecular ions are estimated during the time when the cavity was most pronounced in the density data (5:09:34 UT). (b) Composition ~ 10 min before surge (5:27:14 UT).

At 5:27:14 UT and the same altitudes, there are only hints of remnant molecular ions produced from earlier heating that have not yet combined (the temperature at this time is not elevated). The ion composition estimates from the other cavity events in Figure 1 (not shown) display essentially the same qualitative behavior—enhancements of molecular ions in the F region during the regions of strong heating and relaxation to equilibrium nighttime conditions afterward.

3. Modeling of Observed Density Cavities

A variant of model developed by Zettergren and Semeter [2012] is used to interpret density and heating signatures observed by PFISR during the MICA experiment. This model self-consistently couples a two-dimensional multifluid model (conservation of mass, momentum, and energy) of seven ionospheric species to an electrostatic treatment of auroral currents. All important ionospheric plasma and heat sources (impact ionization, thermal electron heating, and inelastic cooling, thermal conduction, and thermoelectric heat fluxes) are included in the code. For the present study, protons have been included for modeling topside ionospheric effects, and a photoionization module based on Solomon and Qian [2005] has been added. The model equations and numerical methods are described in detail in Zettergren and Semeter [2012, equations 1–5 and 20 and section 2.6].

Recently, the Zettergren and Semeter [2012] model has been adapted to generalized, orthogonal curvilinear coordinates [Zettergren and Snively, 2013]. For the MICA study, we use a dipole coordinate system [e.g., Huba et al., 2000] in which one dimension (denoted x_1) runs along the geomagnetic field lines, the other crosses L shells (denoted x_2). The model resolution may be arbitrarily adjusted (within computing resource constraints), even to include certain types of nonuniform cell sizes. For the simulations in this paper, the grid used spans L shells from $5.85 \leq x_2 \leq 7.6$ and covers altitudes from ~ 80 to 4250 km on a grid of size 243×175 points. The distribution of cells is such that the resolution ($\Delta x_1 \times \Delta x_2$) in the E region is roughly $2 \text{ km} \times 2 \text{ km}$ and in the topside is roughly $75 \text{ km} \times 4 \text{ km}$, adequate resolution for comparing to the ISR data.

Inputs for the Zettergren and Semeter [2012] model are ionospheric field-aligned currents or potential and precipitating electron fluxes, both of which may be spatially and temporally dependent across the top boundary. Dynamo-neutral wind fields can also be input into the model. The model is comparable to many other existing codes [Huba et al., 2000; Noël et al., 2000, 2005; de Boer et al., 2010] but is well suited to this study as it can model the ionosphere at a wide range of latitudes [e.g., Zettergren and Snively, 2013] and ingest a variety of data inputs to realistically specify boundary conditions.

3.1. Data-Driven Boundary Conditions

A novel method for constraining the model described above with combined ISR/Fabry-Perot interferometer (FPI)/rocket data sets has been devised. The four boundary surfaces of the mesh use Dirichlet conditions

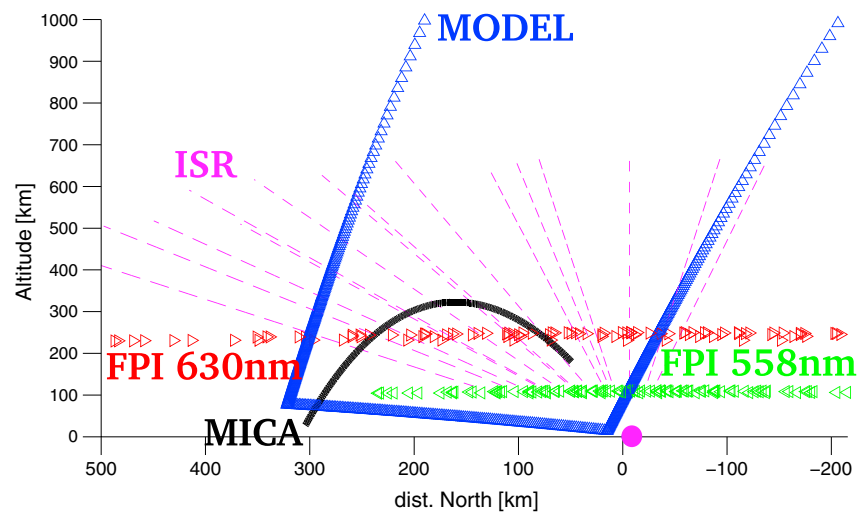


Figure 5. Relation of different data sets used to specify model boundary conditions and source terms. This perspective represents a view from the west of PFISR, which is represented by a magenta, solid circle near the origin of the coordinate system. Dashed lines show the beam positions for the PFISR experiment. Red and green triangles used for the Fabry-Perot interferometer (FPI) data represent individual observation locations with the field of view, and blue triangles used with the model mesh outline show the centers of each cell and illustrate grid spacing.

on the top and sides and zero-current Neumann conditions on the bottom (for the electrostatic equation). The topside potential boundary condition of the model is derived from PFISR perpendicular electric field estimates versus magnetic latitude. This standard data product [Heinselman and Nicolls, 2008] is interpolated onto the mesh, scaled from the measurement altitude to the top boundary, and then integrated numerically to produce a potential versus L shell profile. The side boundaries are taken to be equipotentials with the top “corner” grid points.

Precipitating electron fluxes are estimated by a new method which combines all-sky 427.8 nm emission and scanning Doppler imaging (SDI) measurements (D. L. Hampton, et al., In preparation, 2014). Neutral temperatures fitted from the SDI data are converted to emission altitude by using the MSIS-00 model [Picone et al., 2002]. This emission altitude then sets the characteristic energy of an assumed Maxwellian precipitating electron flux through inversion of the Lummerzheim and Lilensten [1994] suprathermal electron transport model. Finally, this characteristic energy is combined with calibrated 427.8 nm intensity to yield total energy flux through the method of Rees and Luckey [1974]. The SDI neutral wind fields may also be used to specify dynamo, frictional heating, and source current terms in the Zettergren and Semeter [2012] model. Using these data the model then calculates internal electric fields, densities, flows, and temperatures versus time over the entire mesh. Figure 5 shows the spatial relations of the different data sets ingested into the model for the simulations presented below alongside the MICA trajectory. Note that only the remote sensing diagnostics are used to drive the model, while the in situ data are simply compared against the model results in a later section (Figure 11).

Figure 6 shows derived time-dependent quantities used to calculate boundary conditions for the model. The eastward electric field is *not* incorporated into our 2-D model but is shown here for completeness. The electric field activity (Figure 6a) shows intensifications around $\sim 2:40$ – $3:05$ UT (max field of roughly 140 mV/m), $\sim 3:40$ – $4:10$ UT (200 mV/m), $\sim 4:40$ – $5:10$ UT (110 mV/m), $\sim 6:20$ – $6:40$ UT (90 mV/m), and $\sim 7:30$ – $7:45$ UT (100 mV/m). These times also correspond closely to when the cavity events 1–5 are observed. As described below a separate model run is constructed to study each of these density structures. In Figures 6c and 6d, the characteristic energy and total energy flux clearly highlight the substorm surge around 5:40 UT. Note that, due to scattered sunlight, it is not possible to construct reliable estimates for particle characteristic energy and total energy flux prior to $\sim 3:45$ UT. Hence, there are different coverage times for electric fields versus particle fluxes in Figures 6a and 6b versus Figures 6c and 6d.

For modeling of event 3, FPI wind measurements were incorporated into the model using a number of assumptions. The SDI data have been used to compute a single-vector wind measurement averaged over the entire field of view for each of the 557.7 nm and 630.0 nm emissions during this event. These two-vector

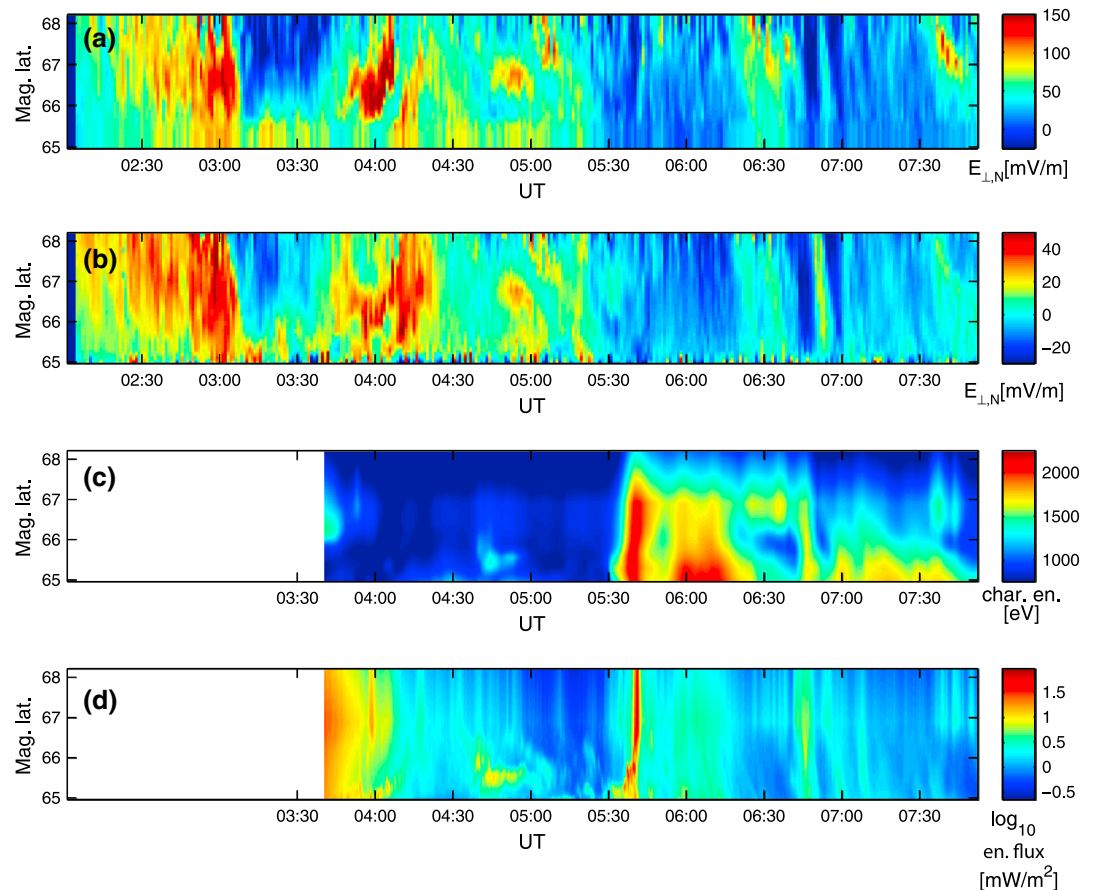


Figure 6. Data used to specify time-dependent model boundary conditions (note that the eastward field is omitted from the model runs). (a) *F* region perpendicular north electric field estimated via PFISR perpendicular plasma drifts. (b) Perpendicular east electric field component (not used in modeling). (c) Characteristic energy estimated from SDI data and suprathermal electron transport model. (d) \log_{10} total energy flux calculated from characteristic energy and calibrated 427.8 nm intensity. All data shown in this figure has been interpolated onto magnetic latitude coordinates of model mesh, i.e., the maximum magnetic latitude shown in these plots corresponds to the northernmost edge of the model mesh (at 300 km altitude) shown in Figure 5. Likewise, the minimum magnetic latitude used in these plots corresponds to the southernmost edge of the mesh (at 300 km altitude).

measurements had values of (110, -280) m/s and (66, -195) m/s, respectively, in geomagnetic north-east coordinates. For purposes of modeling, these winds are assumed to be spatially uniform in the horizontal direction and constant for the duration of event 3. The full time series data indicate that the latter assumption is fairly reasonable. In order to form altitude profiles of the winds for the model, the altitudes of the red and green line emissions were assumed to be 135 km and 230 km, respectively. Wind vectors between these two altitude points were formed by component-wise linear interpolation, above 230 km the winds were assumed constant, and below 135 km the winds were linearly interpolated so that they reached a near zero value at 90 km. Below 90 km the winds were assumed to be negligible.

3.2. Modeled Ionospheric Densities During Cavity Events

Output from the model is examined for times corresponding to the fits presented in Figures 1–3. Results from five different simulations are presented in this article, one for each event identified in the data. The basic configuration and setup for each simulation are as follows. ISR temperature data are examined to identify the time when frictional heating associated with each cavity began. The start time for each model run is then set to 10 min prior to the first observed heating. Initial plasma densities are taken to be consistent with average ISR *F* region values at 10 min prior to first heating. These densities are computed by separate model runs with no auroral forcing since they must be in an equilibrium consistent with background conditions during the experiments. This avoids startup “ringing” due to over/under pressurization of the ionosphere which inevitably occurs when one arbitrarily specifies initial profiles. Initial plasma densities are

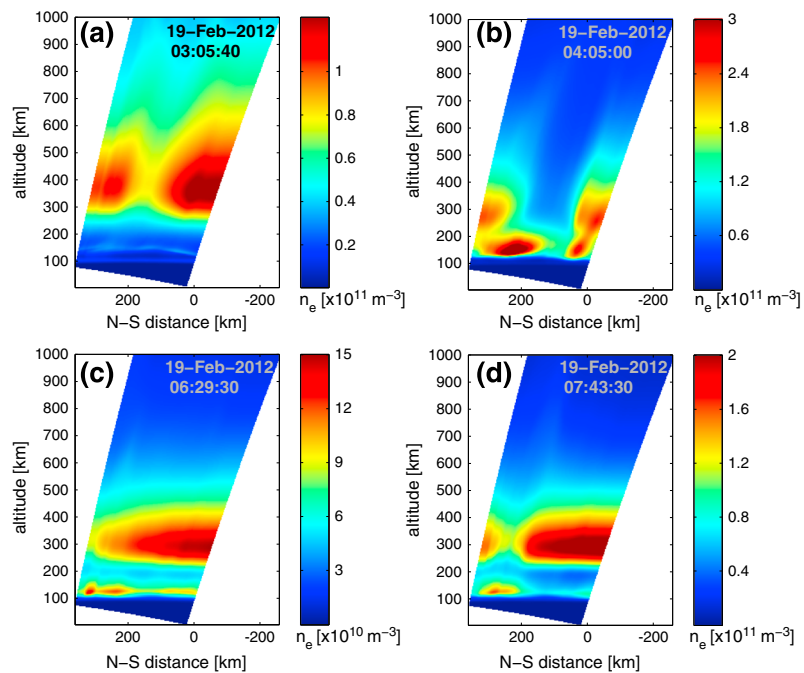


Figure 7. Model densities for the cavity events presented Figure 1 (events 1–2 and 4–5). (a) Event 1 (3:05 UT), (b) event 2 (4:05 UT), (c) event 4 (6:30 UT), and (d) event 5 (7:45 UT). Note that panels of this figure are organized to correspond to those of Figure 1. All model plots show parameters versus *magnetic* N-S distance from PFISR and altitude.

basically horizontally homogeneous (i.e., no density structure exists at the start times). Particles and fields are specified as described above, except for event 1, for which the precipitation estimates are contaminated by scattered sunlight. This event was modeled with a uniform background of ~ 5 keV electrons with total energy flux ~ 0.05 mW/m². As a final note, while the initial conditions have been adjusted to be consistent with the ISR data, no attempt is made to readjust these and rerun the simulations to obtain artificially better agreement with the ISR data.

Figure 7 shows modeling results corresponding to the observations in Figure 1. Overall, the model verifies the formation of density cavities at times when they are present in the ISR data. Modeled temperatures (not shown) are roughly consistent with the ISR fits at this time, as well. Event 2, in particular, is interesting in that the ISR temperature fits and the model results both suggest ion temperatures in excess of 8000 K in the *F* region due to the > 150 mV/m electric field (Figure 6). The cavity features are a reasonable match with the observations of Figure 1. For example, the widest cavity (at 300 km) is event 2 in both the ISR data and simulations. In the ISR data the cavity depths are all between ~ 50 and 80% of the background values (taken outside the frictional heating region), while the model tends to show slightly less intense cavitations of ~ 30 –75%. The deepest depletion in both the ISR and model results is event 2.

The major difference between the model and data is that the modeled cavity locations are not always exactly correct. In Figures 7a and 7b, the cavity occurs in the middle of the model field of view (consistent with observations, compare Figures 1 and 5). However, in Figures 7c and 7d we see the model cavities a bit farther poleward than in the data. This is possibly due to our neglect of zonal electric fields which would drive meridional drifts of the cavities either poleward or equatorward. However, PFISR data suggest that the strongest electric fields are in the meridional direction, and the auroral images indicate roughly planar structures throughout most of the study period. While not yielding perfect agreement with the ISR data, we claim the model is consistent in its ability to recreate the cavities and their basic features.

3.3. The 5 UT Frictional Heating Event (Event 3)

As with the ISR electron density data, the simulated density cavity which preceded the MICA flight (event 3) is examined in detail here. Figures 8a–8c show modeled ionospheric plasma density, ion temperature, and fraction O⁺ at 5:08:50 UT. A deep density depletion is seen near the center of the simulation domain. The depletion is located adjacent to a region of strong electric fields and high ion temperatures ~ 4800 K similar

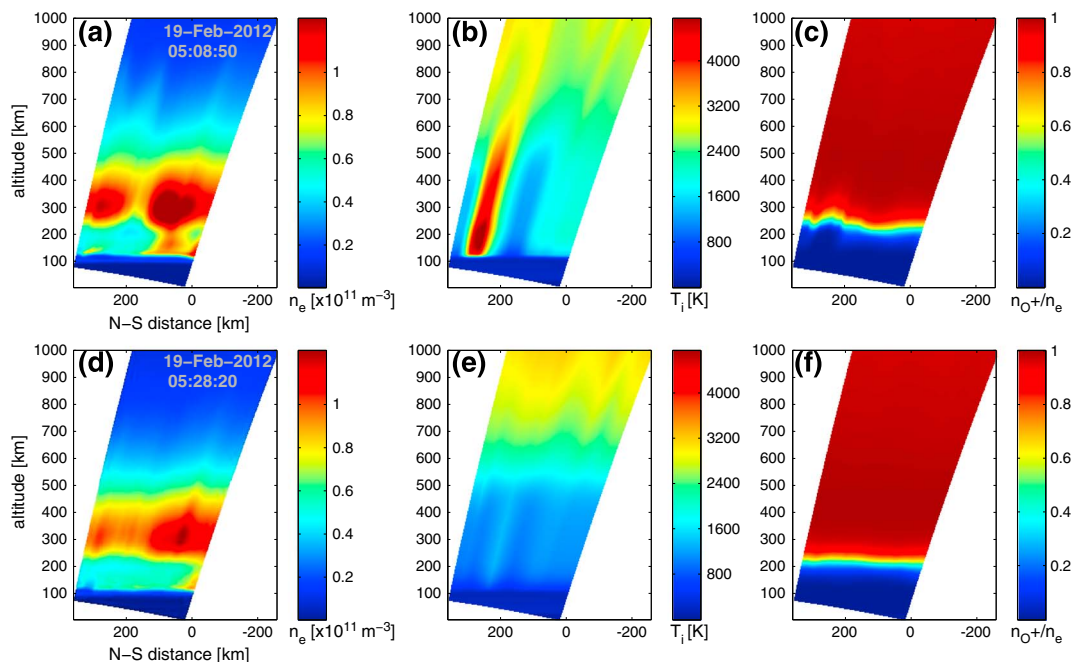


Figure 8. Model results (a–c) during event 3 (5:08:50 UT) and (d–f) ~10 min before launch (5:28:20 UT). Figures 8a and 8d are electron density, Figures 8b and 8e are ion temperature, and Figures 8c and 8f are fraction O^+ .

to those seen in the ISR fits. The density cavity at 300 km altitude is approximately 60% lower than the density maximum toward the south, in both the ISR and simulation results. In Figures 8b and 8e molecular ion enhancements in the regions of high temperatures can be seen. The transition altitude between molecular ions and O^+ (which has a normal nighttime value of ~210 km) is approximately 275 km. These features are also apparent in the analysis of the PFISR data of Figure 4.

Simulation results for 5:28:20 UT are shown in Figures 8d–8f. At this time a density depletion (not as deep as at 5:08 UT) is still apparent in both the model and ISR results. The density in the ISR cavity at 300 km is approximately 50% of the maximum, while the simulation shows a less intense cavity with a 25% depletion. Ion temperatures at this time are nearly at their quiescent nighttime values. In both the ISR fits and model there is only a hint of molecular activity to the northern edge of the field of view/grid.

The electric field-driven ion heating (Figure 6) produces intense field-aligned ion upflows. Since the heating occurred north of the radar, field-aligned flows in these regions are not directly observable. Due to the apparently large perpendicular drifts at this time and large aspect angles of some of the radar beams, the fitted line-of-sight velocities necessarily include large perpendicular components. Figure 9 shows modeled field-aligned velocity (x_1 component, positive “upward,” species averaged) for two times of interest: during

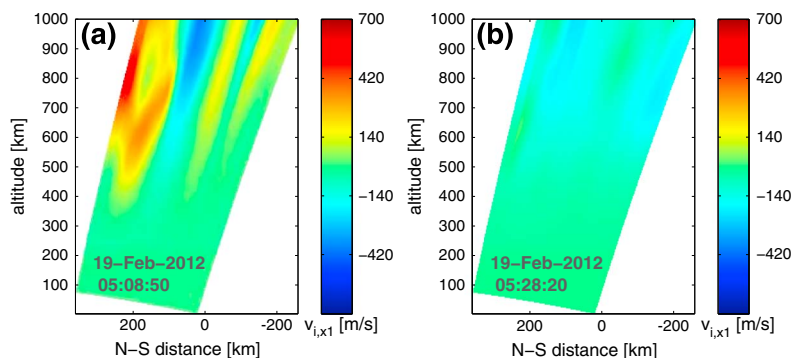


Figure 9. Evolution of ion upflows and downflows around event 3 (a) during active frictional heating (5:08:50 UT) and (b) ~10 min before surge (5:28:20 UT).

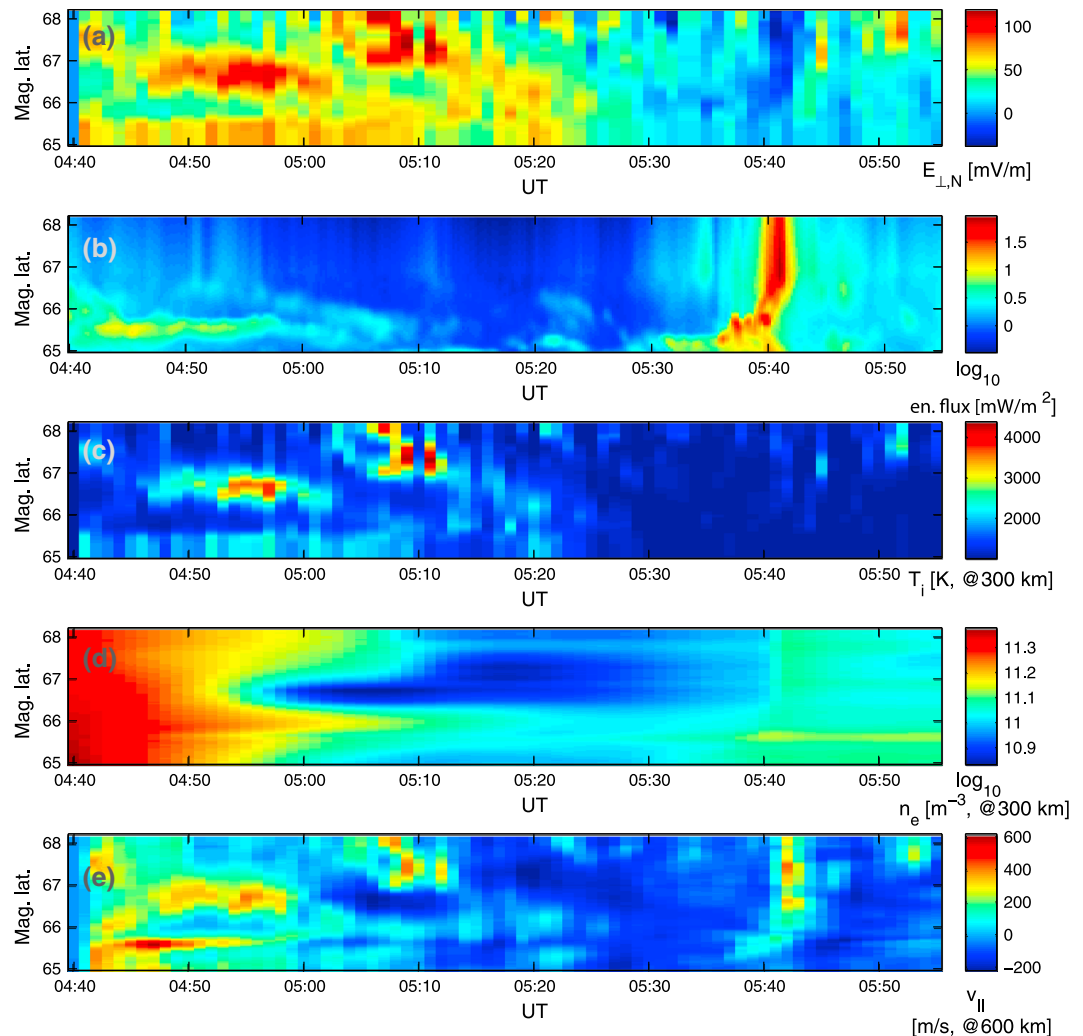


Figure 10. Evolution of modeled plasma parameters around event 3 at fixed altitudes versus magnetic latitude (MLAT) and time. (a) Expanded view (compared to Figure 6) of northward electric field (b) Same but for \log_{10} total energy flux. (c) Species-averaged ion temperature at 300 km altitude. (d) Electron density at 300 km. (e) Average parallel ion velocity.

the active heating and before the flight. For the altitudes shown here, the flows are mostly O^+ , though there are also large proton upflows at altitudes from 1500 to 4000 km at these times. The upflows at 5:08:50 UT (Figure 9a) are due to the ion frictional heating; however, they display substantial structure since the location of the strong electric fields moves with time (Figure 6). This evolving heat source leads to some field lines having both upflow and downflow, an effect which can produce compressional heating of the ions in the topside (see Figure 8b, T_i). Cessation of the frictional heating causes the upward moving plasma stagnate and eventually fall back down, as seen in the 5:28:20 UT results (Figure 9b).

The temporal evolution of event 3 from the model is also shown at a fixed altitude versus time and magnetic latitude in Figure 10. Figures 10a and 10b repeat the event 3 subset of electric field and precipitation estimates for comparison against the model results. Figure 10c shows the ion temperature at 300 km altitude. Frictional heating enhancements are clearly connected to the strong electric fields, both spatially and temporally. Plasma density cavities (Figure 10d) at 300 km are seen to be rather slowly evolving in comparison to the ion temperature. The cavity forming from \sim 4:55 to 5:10 UT which is centered around magnetic latitude 66.75° is a response to the 4:50–5:00 UT heating at this latitude. Higher-latitude heating ($67\text{--}68^\circ$) from 5:05 to 5:10 UT serves to widen the existing cavity in magnetic latitude via erosion of the northern wall of the cavity.

The results shown in Figures 10c, 10d, 8a, and 8b demonstrate an important feature of the ionospheric response to frictional heating. In Figures 8a and 8b (a snapshot at 5:08:50 UT) it is seen that the heating region is displaced from the cavity. The lack of collocation between instantaneous temperature and density is a result of prior heating which produced the density depletion in the center of the mesh. The frictional heating which appears farther to the north has only existed at this intensity in this location for ~ 120 – 180 s (Figure 10). While this is enough time for density to be substantially reduced to the north, it is not enough of a reduction to match the previously generated depletion's depth. Physically, this behavior is due to the fact that molecular ions are quickly produced in the heated regions but require several minutes to recombine and produce the density cavities.

4. Discussion

The detailed information about ion temperature, composition, and density provided by the PFISR results and our comprehensive modeling efforts allows us to examine some of the finer points of the plasma energetics in these auroral cavities. The data in Figures 1–3 represent a scenario consistent with modeling by *Zettergren and Semeter* [2012]. Fitted ion temperatures during these times are similar to those modeled in *Zettergren and Semeter* [2012, Figure 2] and are easily capable of efficiently depleting the F region. Calculations presented in this paper are similar except for the moving heat source (electric field) and bursts of background ionization. It is clear that, even in these more complicated scenarios, molecular ions play a significant role in cavitation. In fact, we can confidently claim that molecular ion generation leading to enhanced recombination is the most important process contributing to the observed depletions during the MICA campaign. To confirm this, all model calculations presented in the previous section have been repeated without including ion temperature and flow velocity effects on chemical reaction rates (i.e., $T_i = T_n$ has been enforced in the simulations). In these modified simulations (not shown) no well-defined cavities form—even though the current closure loss and precipitation are still present.

The cavities seen in the ISR MICA data can all be associated with regions of electric fields exceeding ~ 90 mV/m. PFISR-derived ion temperatures from ~ 4000 to 9000 K are associated with the depletions. Even taking into account possible overestimation due to non-Maxwellian spectra, these temperatures likely still have a maximum of ~ 5000 K—considerably higher than previous PFISR observations of cavity/trough structures [*Zou et al.*, 2013]. It is not clear how common this level of frictional heating is, though there are at least a few other examples in the literature [*Aikio et al.*, 2004; *Zettergren et al.*, 2011].

Density cavities occurring during the MICA experiment occur at nighttime under circumstances qualitatively similar to those observed in *Doe et al.* [1993, 1994]. One trait common to at least the latter four cavity events (for which local all-sky data exist) is that the cavities form adjacent to fairly bright, stationary auroral arcs in a region where the electric fields are strong. Furthermore, almost all of cases presented here have depletions which substantially outlast the frictional heating (Table 1). Hence, the cavities may be a somewhat persistent feature of the nighttime ionosphere, at least in situations resembling those observed by the MICA experiment. It is interesting to note that two of the cavity events, 3 and 4, precede some type of auroral intensification over Poker. Event 3 occurs in the half hour before the $\sim 5:40$ UT substorm expansion, and event 4 precedes the appearance of several north-south auroral streamers above Poker at $\sim 6:41$ UT and $\sim 6:45$ UT (several additional streamers also appear tens of minutes after this). Earlier auroral intensifications, as seen by THEMIS Ground Based Observatory all-sky imagers [*Mende et al.*, 2008], occurred over eastern and central Canada around 3:00 UT and 4:15 UT. Whether the strong electric fields observed over Poker for events 1 and 2 were related to these intensifications is not clear.

4.1. Neutral Wind, Precipitation, and Upflow Influences on Depletions

Neutral winds and precipitation influence cavity dynamics through alteration of ion drifts and impact ionization. Anisotropy in the ion mobilities, thermal electron heating, and upflows make the effects of winds and particles difficult to quantify. Hence, the most straightforward approach is to evaluate their influence by selectively including them in or omitting them from the model. For this exercise, the event 3 simulation results with all inputs (Figures 8 and 9) have been compared against two additional simulations: one with PFISR electric field inputs and winds, and one with only electric field inputs. Results from this exercise show only modest differences between the model calculations of F region density before and during the MICA flight. Regardless of which drivers are included a depletion of 18–25% below “background” forms in the northern half of the model domain ~ 10 min prior to launch.

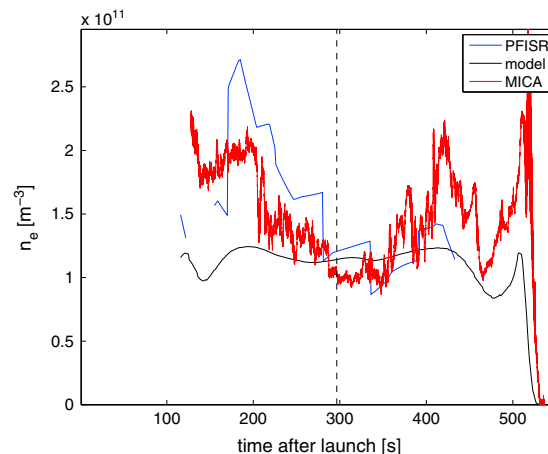


Figure 11. Comparison of PFISR density data, in situ density measured by the MICA sounding rocket and model results. All quantities are plotted versus rocket time of flight. The times plotted in this figure are the same as those used in the trajectory plotted in Figure 5. A vertical dashed line marks time of apogee to facilitate comparison with Figure 5.

in the model results of Figures 9b and 10e. These downflows have typical values of 50–200 m/s in the topside ionosphere (~600–800 km). They persist for much of the time interval between the frictional heating event and the substorm surge (5:15–5:30 UT) and are centered around 67° MLAT (Figure 10e). Detailed examination of the densities in Figure 10d for these times show that the *F* region density in the deepest part of the cavity *increases* by 5–10% owing to downflow refilling. It is also worth noting that this calculation is consistent with the evolution of the density cavity observed by PFISR (Figure 2).

Electron precipitation has a profound effect on the *E* region electron density and temperature throughout the entire model domain. The substorm surge precipitation fills in the cavity, particularly in the bottomside *F* region and gives a modest boost to the peak *F* region density (see Figures 10b and 10d).

In general, the above comments related to downflow and impact ionization refilling indicate that the chemically formed auroral density cavities evolve substantially on fairly long time scales. The depletions seen in the ISR data are actively formed due to heating that lasts ~10–12 min. These cavities continue to slowly refill for the next ~15–20 min, but despite all of the downflow and surge precipitation, low densities persist to the time of the MICA launch (5:41:07 UT), even though *simulated* densities do not strictly satisfy our criteria for a cavity. The phenomenon of density depletions is then one that necessarily involves plasma time history over 0.5–1 h or longer—even for cavities formed “locally” (i.e., not due to structured flow patterns) [Rodger *et al.*, 1992].

4.2. In Situ MICA Density Observations

Results presented in preceding sections may be compared against detailed in situ electron density observations. This exercise serves as another point of verification for the model and also helps evaluate possible effects of spacecraft charging on the rocket measurements. The in situ measurements are at very high space/time resolutions, but the general trends should be consistent with our coarser-scale radar and model results. In order to directly compare ISR and model results to the rocket density measurements, these “data” are trilinearly interpolated onto the rocket path and then sampled in time during the rocket flight using a zero-order hold. Figure 11 shows the ISR, model, and rocket data side-by-side, and illustrates the generally good agreement between densities from the two instruments. The simulation results underestimate the densities but follow many of the same trends in both sets of data. In particular, the generally lower densities in the middle part of the flight ($250 \leq t \leq 350$) are present in all sets of results. The rocket and ISR data match extremely well even though the ISR data are integrated for a full minute for each fit and suggest that spacecraft charging does not greatly affect the in situ measurements. Finally, we note that there is an incredible amount of fine-scale structure in the in situ densities which is not resolved by either of the other

Other plasma parameters show more obvious differences due to inclusion of electron precipitation and winds. Frictional heating due to the northward electric field from ~4:50 to 5:10 UT (cf. Figures 10a and 10c) is suppressed in simulations including the winds, which are antizonal. The maximum ion temperature occurs at ~5:09 UT in all simulations and is ~6000 K without the winds and ~5000 K with them. Moreover, the winds contribute a southward ion drift of ~50 m/s (at the altitude of peak winds), which occurs on top of the mostly northward ion Pedersen drifts from the electric fields. These drifts have the potential to contribute to the plasma depletions if they had enough horizontal structure (they are kept homogeneous in our simulations).

Upflows generated by the 4:55–5:10 UT frictional heating are short-lived, and the downflows that inevitably follow are apparent

methods. These small-scale features and their importance to (magnetosphere-ionosphere coupling are a subject for future investigations [e.g., K. A. Lynch, et al., In preparation, 2014].

4.3. Electron Temperatures and Thermoelectric Effects

Low electron temperatures concurrent with the hot ions have been noted in recent auroral trough observations with the PFISR radar [Zou *et al.*, 2013, and references therein]. These may be related to upward thermoelectric heat fluxes in the DCR, which can represent a substantial heat sink for field-aligned current densities between about $1\text{--}50\ \mu\text{A m}^{-2}$ [Zhang *et al.*, 2003]. However, one must use caution in our experiment due to the large aspect angle of most of the beams. The high ion temperatures at these times imply a non-Maxwellian distribution, which will cause the electron temperature fits to be lower than their actual values. This is one possible explanation for the somewhat low electron temperatures that seem to occur during the ion heating events.

Previous modeling has indicated that the most pronounced thermoelectric cooling is associated with downward currents of $\sim 25\ \mu\text{A m}^{-2}$ [Zhang *et al.*, 2003]. Downward currents that exceed this value saturate and even reverse the thermoelectric cooling through electron drag heating. Our modeling of simple up-down current scenarios (not shown) is consistent with this picture; however, for the MICA simulations, our simulations do not suggest significant electron cooling in the DCR. However, the modeled currents are very sensitive to the scale sizes of the imposed top boundary electric fields and gradients in conductance. Hence, it is entirely possible that electric field and conductivity structures are smaller than what is used in the model (or is resolvable by the ISR), which will typically result in a substantial underestimation of the parallel current density. The alternating code data, while higher resolution, are too noisy to provide any additional information as to the scale sizes of the low electron temperature regions.

5. Summary and Conclusions

In this paper, we have presented a comprehensive case study of the formation, evolution, and decay of auroral density cavities in *F* region. This study is based on a novel framework that combines an updated version of the Zettergren and Semeter [2012] model with optical data from scanning Doppler imagers [Anderson *et al.*, 2011] and filtered all-sky cameras (D. L. Hampton, et al., In preparation, 2014) and PFISR data. These data constrain the model boundary and initial conditions—normally the main hindrance in providing detailed quantitative modeling results. These simulations, along with the PFISR-fitted results provide coarse spatial scale (tens of kilometers) contextual information critical to interpreting the fine-scale measurements made from rocket platforms (MICA in this case) (K. A. Lynch, et al., In preparation, 2014).

Comparison of ISR cavity observations with modeled density depletions shows reasonable agreement and serves as a type of validation for the Zettergren and Semeter [2012] model. As discussed in their paper, for medium scale current systems ($\sim 20\ \text{km}$ perpendicular to the geomagnetic field), the chemical cavitation process is dominant for producing *F* region depletions for very strong frictional heating. This conclusion holds for the more detailed studies presented here which also include the effects of realistic impact ionization, winds, and spatiotemporally variable inputs. Whether it is valid for events with weaker heating remains to be seen. Quantitative investigations of the combined effects of the “local” arc-related depletion processes considered here (divergent Pedersen drifts, recombination, and ion upflow) and their relation to plasma density structures formed through structured $\mathbf{E} \times \mathbf{B}$ convection will apparently require a fully three-dimensional modeling approach (ideally constrained by data). Indeed, some of our volumetric observations of the density cavities show significant structure along the third dimension, the magnetic zonal direction (e.g., Figure 2), and also hint at the presence of $\mathbf{E} \times \mathbf{B}$ drift effects on the cavities.

Our detailed simulations show that background neutral winds and transient ion upflows and downflows provide important modulations in cavity evolution. Observed neutral winds are shown to suppress the frictional heating and formation of the cavities. However, they are not strong enough to greatly impede cavity formation in event 3. Upflows remove a fair bit of plasma from the *F* region and topside, but downflows that accompany the cessation of heating inevitably partially refill the plasma loss. It is interesting to note that if any ion energization and outflow occurs above these regions that the downflow refilling process will be reduced in effectiveness. Intermittent, intense particle precipitation also refills the cavities through impact ionization.

For the cavities observed in the ISR data, the molecular ion estimates produced from the method of Richards *et al.* [2010] are consistent with detailed modeling and other estimation schemes [Blclly *et al.*, 2010; Zettergren *et al.*, 2011]. This method deserves further analysis, but its apparent success here is a promising sign for future attempts to address ion temperature/mass ambiguities in IS spectral analysis. As with other recently developed methods, it is almost certainly preferable to using a composition profile which includes only average diurnal and seasonal variations. Non-Maxwellian spectra continue to pose a serious problem for interpreting data from the AMISR (Advanced Modular Incoherent Scatter Radar) systems, as exemplified in the data presented in this report. Scan geometries for these radars inevitably involve large aspect angles in order to get better spatial coverage. To get accurate plasma parameters in these experiments, a non-Maxwellian model needs to be developed for future studies. Our modeling has elucidated some of the energetics of cavity formation and evolution, but a more detailed assessment capable of clarifying the range of frictional heating in these cavities and DCR thermoelectric cooling processes will have to await a non-Maxwellian analysis and/or further modeling studies.

Acknowledgments

The MICA project is dedicated to the memory of Paul M. Kintner Jr., its original principal investigator. M. Zettergren and B. Wright acknowledge the support of NSF CAREER grant AGS-1255181 and NSF grant AGS-1000302. K. Lynch and D. Hampton were supported by NASA grants NNX10AL18G and NNX10AL20G, respectively. The Poker Flat Incoherent Scatter Radar is operated by SRI International on behalf of the NSF under NSF Cooperative agreement AGS-1133009. M.Z. also thanks ISSI in Bern, Switzerland, for supporting this work through hosted meetings. ISR data used in this paper are available for download from the CEDAR/Madrigal database <http://isr.sri.com/madrigal/>. They are also available from the SRI ISR website <http://amisr.com/amisr/links/data-access/>. In situ electron density data and characteristic energy and total energy flux estimates may be obtained by email request to the corresponding author (M. Zettergren, zettergm@erau.edu). Model output used in this study can also be reproduced and made available upon request to the corresponding author.

Robert Lysak thanks Yi-Jiun Su and Anita Aikio for their assistance in evaluating this paper.

References

- Aikio, A., K. Mursula, S. Buchert, F. Forme, O. Amm, G. Marklund, M. Dunlop, D. Fontaine, A. Vaivads, and A. Fazakerley (2004), Temporal evolution of two auroral arcs as measured by the Cluster satellite and coordinated ground-based instruments, *Ann. Geophys.*, *22*, 4089–4101, doi:10.5194/angeo-22-4089-2004.
- Akbari, H., J. L. Semeter, H. Dahlgren, M. Diaz, M. Zettergren, A. Strømme, M. J. Nicolls, and C. Heinselman (2012), Anomalous ISR echoes preceding auroral breakup: Evidence for strong Langmuir turbulence, *Geophys. Res. Lett.*, *39*, L03102, doi:10.1029/2011GL050288.
- Anderson, C., T. Davies, M. Conde, P. Dyson, and M. J. Kosch (2011), Spatial sampling of the thermospheric vertical wind field at auroral latitudes, *J. Geophys. Res.*, *116*, A06320, doi:10.1029/2011JA016485.
- Anderson, P. C., R. A. Heelis, and W. B. Hanson (1991), The ionospheric signatures of rapid subauroral ion drifts, *J. Geophys. Res.*, *96*, 5785–5792, doi:10.1029/90JA02651.
- Blclly, P.-L., D. Alcaydé, and A. P. van Eyken (2010), A new analysis method for determining polar ionosphere and upper atmosphere characteristics from ESR data: Illustration with IPY period, *J. Geophys. Res.*, *115*, A09322, doi:10.1029/2009JA014876.
- Brinton, H. C., J. M. Grebowsky, and L. H. Brace (1978), The high-latitude winter *F* region at 300 km: Thermal plasma observations from AE-C, *J. Geophys. Res.*, *83*, 4767–4776, doi:10.1029/JA083iA10p04767.
- Collis, P. N., and I. Haggstrom (1988), Plasma convection and auroral precipitation processes associated with the main ionospheric trough at high latitudes, *J. Atmos. Terr. Phys.*, *50*, 389–404.
- Cran-McGreehin, A. P., A. N. Wright, and A. W. Hood (2007), Ionospheric depletion in auroral downward currents, *J. Geophys. Res.*, *112*, A10309, doi:10.1029/2007JA012350.
- de Boer, J. D., J.-M. A. Noël, and J.-P. St.-Maurice (2010), The effects of mesoscale regions of precipitation on the ionospheric dynamics, electrodynamic and electron density in the presence of strong ambient electric fields, *Ann. Geophys.*, *28*, 1345–1360, doi:10.5194/angeo-28-1345-2010.
- Diloy, P.-Y., A. Robineau, J. Liliensten, P.-L. Blclly, and J. Fontanari (1996), A numerical model of the ionosphere, including the E-region above EISCAT, *Ann. Geophys.*, *14*, 191–200.
- Doe, R. A., M. Mendillo, J. F. Vickrey, L. J. Zanetti, and R. W. Eastes (1993), Observations of nightside auroral cavities, *J. Geophys. Res.*, *98*, 293–310, doi:10.1029/92JA02004.
- Doe, R. A., M. Mendillo, J. F. Vickrey, J. M. Ruohoniemi, and R. A. Greenwald (1994), Coordinated convection measurements in the vicinity of auroral cavities, *Radio Sci.*, *29*, 293–309, doi:10.1029/93RS02129.
- Doe, R. A., J. F. Vickrey, and M. Mendillo (1995), Electrodynamic model for the formation of auroral ionospheric cavities, *J. Geophys. Res.*, *100*, 9683–9696, doi:10.1029/95JA00001.
- Evans, J. (1969), Theory and practice of ionosphere study by Thomson scatter radar, *Proc. IEEE*, *57*(4), 496–530.
- Evans, J. V., J. M. Holt, W. L. Oliver, and R. H. Wand (1983), The fossil theory of nighttime high latitude *F* region troughs, *J. Geophys. Res.*, *88*, 7769–7782, doi:10.1029/JA088iA10p07769.
- Grebowsky, J. M., H. A. Taylor Jr., and J. M. Lindsay (1983), Location and source of ionospheric high latitude troughs, *Planet. Space Sci.*, *31*, 99–105, doi:10.1016/0032-0633(83)90034-X.
- Haggstrom, I., and P. N. Collis (1990), Ion composition changes during *F*-region density depletions in the presence of electric fields at auroral latitudes, *J. Atmos. Terr. Phys.*, *52*, 519–529.
- Heinselman, C. J., and M. J. Nicolls (2008), A Bayesian approach to electric field and E-region neutral wind estimation with the Poker Flat Advanced Modular Incoherent Scatter Radar, *Radio Sci.*, *43*, RS5013, doi:10.1029/2007RS003805.
- Huba, J. D., G. Joyce, and J. A. Fedder (2000), Sami2 is Another Model of the Ionosphere (SAMI2): A new low-latitude ionosphere model, *J. Geophys. Res.*, *105*, 23,035–23,054, doi:10.1029/2000JA000035.
- Hubert, D., and C. Lathuillere (1989), Incoherent scattering of radar waves in the auroral ionosphere in the presence of high electric fields, and measurement problems with the EISCAT facility, *J. Geophys. Res.*, *94*, 3653–3662, doi:10.1029/JA094iA04p03653.
- Karlsson, T., G. T. Marklund, L. G. Blomberg, and A. Mälkki (1998), Subauroral electric fields observed by the Freja satellite: A statistical study, *J. Geophys. Res.*, *103*, 4327–4342, doi:10.1029/97JA00333.
- Karlsson, T., G. T. Marklund, N. Brenning, and I. Afnas (2005), On enhanced aurora and low-altitude parallel electric fields, *Phys. Scr.*, *72*, 419–422, doi:10.1238/Physica.Regular.072a00419.
- Kelly, J. D., and V. B. Wickwar (1981), Radar measurements of high-latitude ion composition between 140 and 300 km altitude, *J. Geophys. Res.*, *86*, 7617–7626.
- Knudsen, W. C. (1974), Magnetospheric convection and the high-latitude *F*₂ ionosphere, *J. Geophys. Res.*, *79*, 1046, doi:10.1029/JA079i007p01046.
- Lummerzhim, D., and J. Liliensten (1994), Electron transport and energy degradation in the ionosphere: Evaluation of the numerical solution, comparison with laboratory experiments and auroral observations, *Ann. Geophys.*, *12*, 1039–1051, doi:10.1007/s00585-994-1039-7.

- Lysak, R. L., and Y. Song (2002), Energetics of the ionospheric feedback interaction, *J. Geophys. Res.*, *107*(A8), 1160, doi:10.1029/2001JA000308.
- Marklund, G. T. (2009), Electric fields and plasma processes in the auroral downward current region, below, within, and above the acceleration region, *Space Sci. Rev.*, *142*, 1–21, doi:10.1007/s11214-008-9373-9.
- McFarland, M., D. L. Albritton, F. C. Fehsenfeld, E. E. Ferguson, and A. L. Schmeltekopf (1973), Flow-drift technique for ion mobility and ion-molecule reaction rate constant measurements. II. Positive ion reactions of N^+ , O^+ , and H_2^+ with O_2 and O^+ with N_2 from thermal to ~ 2 eV, *J. Chem. Phys.*, *59*, 6620–6628.
- Mende, S. B., S. E. Harris, H. U. Frey, V. Angelopoulos, C. T. Russell, E. Donovan, B. Jackel, M. Greffen, and L. M. Peticolas (2008), The THEMIS array of Ground-Based Observatories for the study of auroral substorms, *Space Sci. Rev.*, *141*, 357–387, doi:10.1007/s11214-008-9380-x.
- Moffett, R. J., and S. Quegan (1983), The mid-latitude trough in the electron concentration of the ionospheric F-layer: A review of observations and modelling, *J. Atmos. Terr. Phys.*, *45*, 315–343.
- Nilsson, H., A. Kozlovsky, T. Sergienko, and A. Kotikov (2005), Radar observations in the vicinity of pre-noon auroral arcs, *Ann. Geophys.*, *23*, 1785–1796, doi:10.5194/angeo-23-1785-2005.
- Noël, J.-M. A., J.-P. St.-Maurice, and P.-L. Blelly (2000), Nonlinear model of short-scale electrodynamic in the auroral ionosphere, *Ann. Geophys.*, *18*, 1128–1144, doi:10.1007/s00585-000-1128-1.
- Noël, J.-M. A., J.-P. St.-Maurice, and P.-L. Blelly (2005), The effect of E-region wave heating on electrodynamic structures, *Ann. Geophys.*, *23*, 2081–2094, doi:10.5194/angeo-23-2081-2005.
- Picone, J. M., A. E. Hedin, D. P. Drob, and A. C. Aikin (2002), NRLMSISE-00 empirical model of the atmosphere: Statistical comparisons and scientific issues, *J. Geophys. Res.*, *107*, 1468, doi:10.1029/2002JA009430.
- Raman, R. S. V., J. P. St.-Maurice, and R. S. B. Ong (1981), Incoherent scattering of radar waves in the auroral ionosphere, *J. Geophys. Res.*, *86*, 4751–4762, doi:10.1029/JA086iA06p04751.
- Rees, M. H., and D. Luckey (1974), Auroral electron energy derived from ratio of spectroscopic emissions. I. Model computations, *J. Geophys. Res.*, *79*, 5181–5186, doi:10.1029/JA079i034p05181.
- Richards, P. G., D. Bilitza, and D. Voglozin (2010), Ion density calculator (IDC): A new efficient model of ionospheric ion densities, *Radio Sci.*, *45*, R55007, doi:10.1029/2009RS004332.
- Rodger, A. S., R. J. Moffett, and S. Quegan (1992), The role of ion drift in the formation of ionisation troughs in the mid- and high-latitude ionosphere—A review, *J. Atmos. Terr. Phys.*, *54*, 1–30.
- Russell, A. J. B., A. N. Wright, and A. V. Streltsov (2013), Production of small-scale Alfvén waves by ionospheric depletion, nonlinear magnetosphere-ionosphere coupling and phase mixing, *J. Geophys. Res. Space Physics*, *118*, 1450–1460, doi:10.1002/jgra.50168.
- Schunk, R. W. (1977), Mathematical structure of transport equations for multispecies flows, *Rev. Geophys. Space Phys.*, *15*, 429–445.
- Schunk, R. W., and J. J. Sojka (1987), A theoretical study of the lifetime and transport of large ionospheric density structures, *J. Geophys. Res.*, *92*, 12,343–12,351, doi:10.1029/JA092iA11p12343.
- Schunk, R. W., P. M. Banks, and W. J. Raitt (1975), Effect of electric fields on the daytime high-latitude E and F regions, *J. Geophys. Res.*, *80*, 3121–3130.
- Sojka, J. J., W. J. Raitt, and R. W. Schunk (1981a), A theoretical study of the high-latitude winter F region at solar minimum for low magnetic activity, *J. Geophys. Res.*, *86*, 609–621, doi:10.1029/JA086iA02p00609.
- Sojka, J. J., W. J. Raitt, and R. W. Schunk (1981b), Plasma density features associated with strong convection in the winter high-latitude F region, *J. Geophys. Res.*, *86*, 6908–6916, doi:10.1029/JA086iA08p06908.
- Solomon, S. C., and L. Qian (2005), Solar extreme-ultraviolet irradiance for general circulation models, *J. Geophys. Res.*, *110*, A10306, doi:10.1029/2005JA011160.
- St.-Maurice, J.-P., and P. J. Laneville (1998), Reaction rate of O^+ with O_2 , N_2 , and NO under highly disturbed auroral conditions, *J. Geophys. Res.*, *103*, 17,519–17,522.
- St.-Maurice, J.-P., and D. G. Torr (1978), Nonthermal rate coefficients in the ionosphere—The reactions of O^+ with N_2 , O_2 , and NO, *J. Geophys. Res.*, *83*, 969–977, doi:10.1029/JA083iA03p00969.
- Streltsov, A. V., and T. Karlsson (2008), Small-scale, localized electromagnetic waves observed by Cluster: Result of magnetosphere-ionosphere interactions, *Geophys. Res. Lett.*, *35*, L22107, doi:10.1029/2008GL035956.
- Streltsov, A. V., and W. Lotko (2004), Multiscale electrodynamic of the ionosphere-magnetosphere system, *J. Geophys. Res.*, *109*, A09214, doi:10.1029/2004JA010457.
- Streltsov, A. V., and W. Lotko (2008), Coupling between density structures, electromagnetic waves and ionospheric feedback in the auroral zone, *J. Geophys. Res.*, *113*, A05212, doi:10.1029/2007JA012594.
- Torr, M. R., D. G. Torr, and J. P. Saint-Maurice (1977), The rate coefficient for the $O^+ + N_2$ reaction in the ionosphere, *J. Geophys. Res.*, *82*, 3287–3290.
- Wilson, G. R., and P. Craven (1999), Molecular ion upflow in the cleft ion fountain, *J. Geophys. Res.*, *104*, 4437–4446, doi:10.1029/1998JA900070.
- Winsor, K. J., G. O. L. Jones, and P. J. S. Williams (1986), A quantitative study of the high latitude ionospheric trough using EISCAT's common programmes, *J. Atmos. Terr. Phys.*, *48*, 893–904.
- Zettergren, M., and J. Semeter (2012), Ionospheric plasma transport and loss in auroral downward current regions, *J. Geophys. Res.*, *117*, A06306, doi:10.1029/2012JA017637.
- Zettergren, M., and J. Snively (2013), Ionospheric signatures of acoustic waves generated by transient tropospheric forcing, *Geophys. Res. Lett.*, *40*, 5345–5349, doi:10.1002/2013GL058018.
- Zettergren, M., J. Semeter, B. Burnett, W. Oliver, C. Heinselman, P.-L. Blelly, and M. Diaz (2010), Dynamic variability in F-region ionospheric composition at auroral arc boundaries, *Ann. Geophys.*, *28*, 651–664, doi:10.5194/angeo-28-651-2010.
- Zettergren, M., J. Semeter, C. Heinselman, and M. Diaz (2011), Incoherent scatter radar estimation of F region ionospheric composition during frictional heating events, *J. Geophys. Res.*, *116*, A01318, doi:10.1029/2010JA016035.
- Zhang, B.-C., Y. Kamide, and R.-Y. Liu (2003), Response of electron temperature to field-aligned current carried by thermal electrons: A model, *J. Geophys. Res.*, *108*(A5), 1169, doi:10.1029/2002JA009532.
- Zou, S., M. B. Moldwin, M. J. Nicolls, A. J. Ridley, A. J. Coster, E. Yizengaw, L. R. Lyons, and E. F. Donovan (2013), Electrodynamics of the high-latitude trough: Its relationship with convection flows and field-aligned currents, *J. Geophys. Res. Space Physics*, *118*, 2565–2572, doi:10.1002/jgra.50120.